https://doi.org/10.5194/egusphere-2025-3068
Preprint. Discussion started: 14 July 2025

A Source or a Sink? How Trends in Particle Precipitation Dictate Electrodynamics in High-Latitude Ionosphere

Magnus F Ivarsen[1,2]

[1]Department of Physics and Engineering Physics, University of Saskatchewan, Saskatoon, Canada
[2]The European Space Agency Centre for Earth Observation, Frascati, Italy

Correspondence: magnus.fagernes@gmail.com

Abstract. Fast, charged particles intermittently rain down into Earth's dense atmosphere. The kinetic energy of these particles are converted into heat and light, and it ionizes the atmospheric gas, providing a source of both free and bound energy for the ionosphere; this is the *aurora borealis* and *australis*. The specific kinetic energy of the constituent particles in the aurora dictates the atmospheric response to the ongoing particle precipitation, with hard (*high*-energy) particles penetrating deeper than those that are considered soft (possessing a low kinetic energy). In this paper, we analyze a large database of precipitating particle observations from the United States' Defense Meteorological Satellite Program, and aggregate the altitude-dependent response of the ionosphere at high-latitudes, using fast ionization rate parameterizations due to two important papers by Fang et al. (`10.1029/2010GL045406` and `10.1002/jgra.50484`). We explore a characteristic altitude-dependent pattern in space (magnetic latitude and longitude), and time (geomagnetic activity), pertaining to the shape of the northern hemisphere, high-latitude ionosphere during local winter. We briefly discuss the implied ratio of E- to F-region Pedersen conductance, and this ratio's ramifications for the growth & decay (and thus proliferation) of plasma turbulence in the high-latitude ionosphere.

1 Introduction

The most prominent feature of geospace is the constant pushing of the solar wind against Earth's extended magnetic presence, the magnetosphere (Cowley, 2000). A basic two-cell convection pattern is the large scale result that is imparted on the ionosphere at high latitudes, in which plasma drifts, or convects, from the dayside to the nightside (Thomas and Shepherd, 2018).

Imposed on this large-scale pattern is an attendant, mostly diffuse, pattern of particle precipitation (Newell et al., 2009, 2010). Primarily, this pattern is created by orbiting electrons whose trajectories are nudged by plasma waves so that they rain down along Earth's field-lines into the atmosphere (Thorne et al., 2010; Kasahara et al., 2018), and to a lesser extent it is created by electrons that are accelerated downwards by parallel electric fields (Borovsky et al., 2019; Lysak et al., 2020).

Regardless of the causes, precipitating particles are stopped by the atmosphere in rates that are decided by the kinetic energy of the particles themselves, as well as the chemical composition of the atmospheric gas (air). The impacting particles ionize the gas, and so the density and molecular composition of the atmosphere lead to characteristic altitude-profiles of ionization

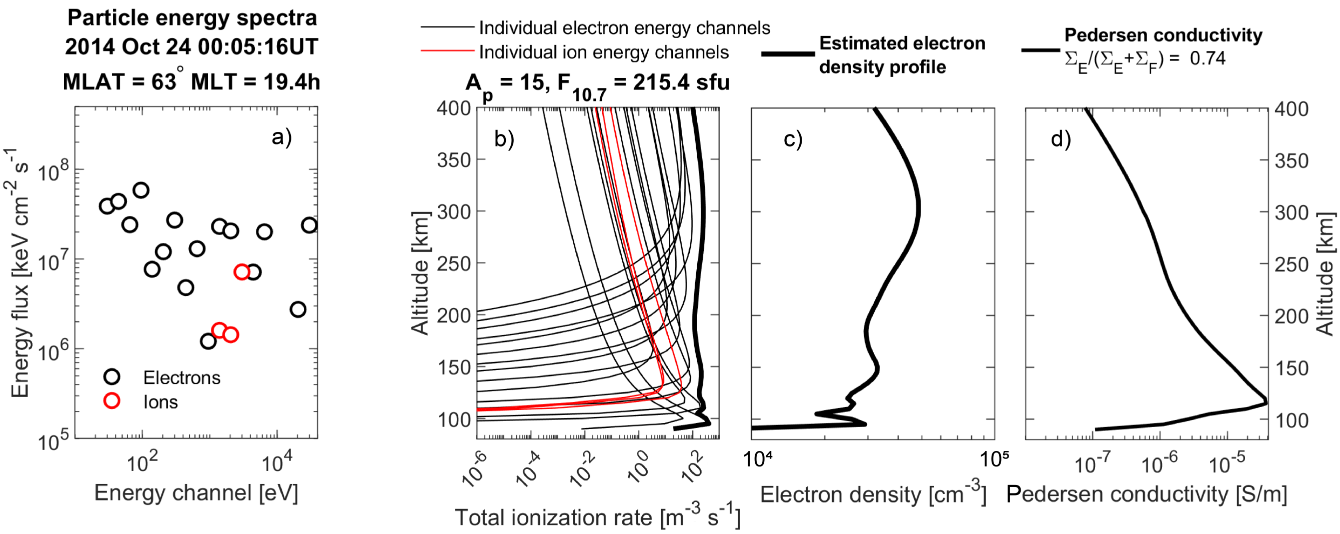

Figure 1. Panel a): a precipitating electron (black circles) and ion (red circles) spectrum observed by the DMSP F18 satellite on 24 October 2014. **Panel b):** the ionization rate altitude profiles based on the spectra, using the equations published by Fang et al. (2010) and Fang et al. (2013), together with the MSIS (Picone et al., 2002) model for the neutral atmosphere composition and the IGRF (Alken et al., 2021) model for magnetic field strengths. Solar and geomagnetic activity, for which the MSIS model is dependent, is indicated by the A_p- and $F_{10.7}$-indices. **Panel c):** Estimated plasma density profile, assuming that NO_+ dominates in the E-region, balancing production (ionization rate) with loss (recombination) (absent of solar EUV photoionization), under the assumption of a Chapman function above the F-peak. **Panel d):** Estimated conductivities resulting from particle collision interaction terms (Schunk and Nagy, 1980), using modelled compositions due to MSIS and IGRF. The ratio of E- to F-region conductance is indicated. See the supporting information for a more thorough description.

rate. Notably, Fang et al. (2010) and Fang et al. (2013) presented parameterizations of time-consuming non-linear models of such ionization rate altitude profiles, enabling the fast calculation of millions of datapoints in aggregate.

2 Motivation

Figure 1 shows an implementation of those equations to an example pair of precipitating electron and ion spectra, following the the increased ionization rate in a natural path towards increased plasma density in the ionosphere, and consequent enhancements in *conductance*, the ability of the ionosphere to support electrical currents (Prölss, 2004a, b), culminating in the calculation of,

$$\eta \equiv \frac{\Sigma_E}{\Sigma_E + \Sigma_F}, \tag{1}$$

where $\Sigma_{E,F}$ represents conductance (height-integrated conductivity) in the E- and F-regions respectively. While the profiles in Figure 1c–d) are useful, their analysis must be precluded by a clear admission of simplification by several assumptive steps (see Figure 1 caption and the Appendix A).

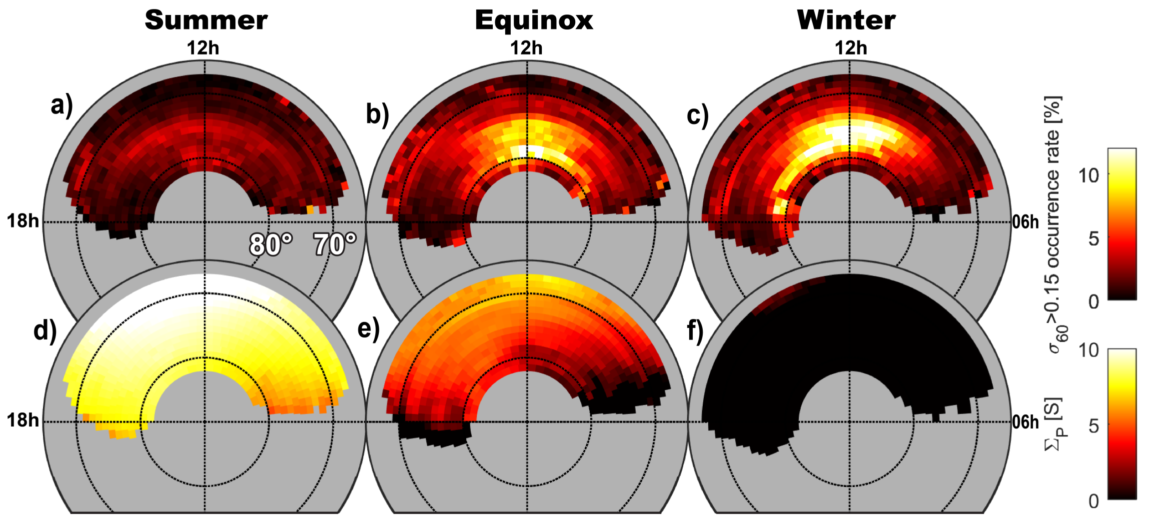

Figure 2. A dayside climatology of GNSS scintillations (panels a-c), and a dayside climatology of Pedersen conductance induced by solar EUV photoionization (panels d-f), for the high-latitude (Magnic Latitude, or MLAT, $> 68°$) northern hemisphere. Phase scintillation events are recorded with ground-based receivers in Svalbard, Norway, and Conductance levels are calculated with an SZA-based model due to Moen and Brekke (1993), namely, $\Sigma_E = (F_{10.7})^{0.49}\left(0.34\cos Z + 0.93\cos^{1/2} Z\right)$. The data is aggregated in field-line-traced (altitude-corrected) geomagnetic coordinates (Baker and Wing, 1989), where magnetic noon is at the top and dusk to the right, and where we assume that the observed Pedersen conductance is located where Pedersen conductivity typically maximizes near 130 km (Kwak and Richmond, 2007). ’Summer’ and ’winter’ are calculated based on a 131-day window centered on the respective solstices, while ’Equinox’ describes the rest of the data, dividing the calendar year into roughly three equal parts. Note that the prominent “hot spot" of phase scintillations near magnetic noon is caused by the magnetospheric cusp (see, e.g., Ivarsen et al., 2023).

Returning to the topic at hand, we note that the impacting particle precipitation that precluded Figure 1 is an intermittent and highly localized phenomenon. Overall, the main source of energy for the ionosphere stem directly from our Sun, whose extreme ultraviolet (EUV) radiation maintains a strong, steady-state, partial (< 1 %) ionization of the entire dayside atmosphere. The factors of importance in the case of solar EUV radiation is the solar zenith angle, the angle between Earth’s surface and a vector connecting the observer to the centre of our Sun, Z, as well as the $F_{10.7}$-index, the quantified 10.7 cm solar radio flux (Moen and Brekke, 1993). Figure 2d–f) show the estimated conductance of the ionosphere in three seasonal bins, highlighting how the turning of the seasons lead to drastic changes to the ionosphere’s ability to support currents.

Also shown in Figure 2, in panels a–c, are the occurrence rate of radio phase scintillations above Svalbard, Norway, for the same three seasonal bins. Such disturbances, called GNSS (Global Navigational Satellite System) phase scintillations, are defraction of the radio signal as it passes through kilometer-scale gradients in plasma density, or more generally, plasma irregularities Yeh and Liu (1982); Kintner P. M. et al. (2007); Song et al. (2023); Meziane et al. (2023). In Figure 2, we readily observe that whereas high-latitude conductance maximizes during local summer, the occurrence of plasma irregularities maximizes during local winter, with both quantities displaying a severe contrast between the two extrema. An important reason

https://doi.org/10.5194/egusphere-2025-3068
Preprint. Discussion started: 14 July 2025

for these strong, opposing trends is the ability of a conducting ionosphere to *short-circuit* the electric field that drives plasma instabilities (Vickrey and Kelley, 1982). The mechanism is well-studied and has been illuminated by, e.g., Kivanc and Heelis (1998), Prikryl et al. (2015), and Ivarsen et al. (2019).

The above considerations carry the important implication that the intermittent ionization caused by aurorae is of utmost importance for plasma dynamics in the dark, high-latitude ionosphere, which is otherwise largely non-conducting, providing motivation for the present study into ionospheric electrodynamics. In the absence of solar EUV ionization, particle precipitation is directly associated with both the growth and the decay of plasma irregularities, but the relationship between growth and decay is under debate (Ivarsen et al., 2021b, 2024b). Here, the characteristics of the precipitating particles themselves, as well as the state of Earth's outer atmosphere, is key to understand the behaviour of an externally driven ionosphere.

In the present paper, we analyze a large database of precipitating particle observations from the SSJ-instrument (Redmon et al., 2017) onboard the many satellites belonging the United States' Defense Meteorological Satellite Program (DMSP). We apply the fast parameterizations due to Fang et al. (2010) and Fang et al. (2013), and examine the average ionization rate altitude profiles that are characteristic to geomagnetic activity at various magnetic local times. We discuss the inferred, or estimated, ratio of E-region (bottomside) to F-region (topside) conductance, and how this ratio should affect the many observations that have been made of plasma irregularities in the high-latitude ionosphere.

The above is achieved by presenting three specialized analyses (Figures 3–5), each segmenting the estimated ionospheric response to particle precipitation by spatial (geomagnetic coordinates) and temporal (geomagnetic activity) bins, using data from the northern hemisphere winter, when overall conductivity is low. The efforts are not intending to present a general-statistical climatology, but are rather implemented to expose a characteristic behaviour of the high-latitude ionosphere, whose intrinsic implications demand our attention.

3 Some Trends

Figure 3 shows the first of the curious trends that we expose in the present paper. We bin some 5 million precipitating particle spectra observed by all four DMSP satellites in the dawn- and pre-noon section of the northern hemisphere, collected during the local winter seasons of 2014–2016 (with winter defined as a 131-day period centered on the December solstice). In this region, spanning magnetic local times between 4h and 11h, the satellites achieve excellent coverage, avoiding both the narrow gap centered around noon at lower latitudes and the wide gap centered on midnight. The figure shows a distinct magnetic local time-trend that occurs during disturbed conditions. The collected precipitating particle spectra (Figure 3a) imply a systematic organization of ionization rate by altitude (Figure 3b), which in fact defines the shape of the ionosphere's bottomside; with increased levels of particle precipitation, the ionosphere *sags* towards midnight, where significant ionization (and free energy) is injected into the E-region. The result is a drastic decrease in the ratio of ionization experienced by the bottomside compared to the topside, as magnetic local time approaches noon (Figure 3c). The last two panels of Figure 3 explores how the above basic mechanism evolves in time, through changes in geomagnetic activity and interplanetary magnetic field configuration. Figure 3c) shows absolute changes in ionization rate implied by the DMSP-observed particle spectra, using a red-blue colorscale, where

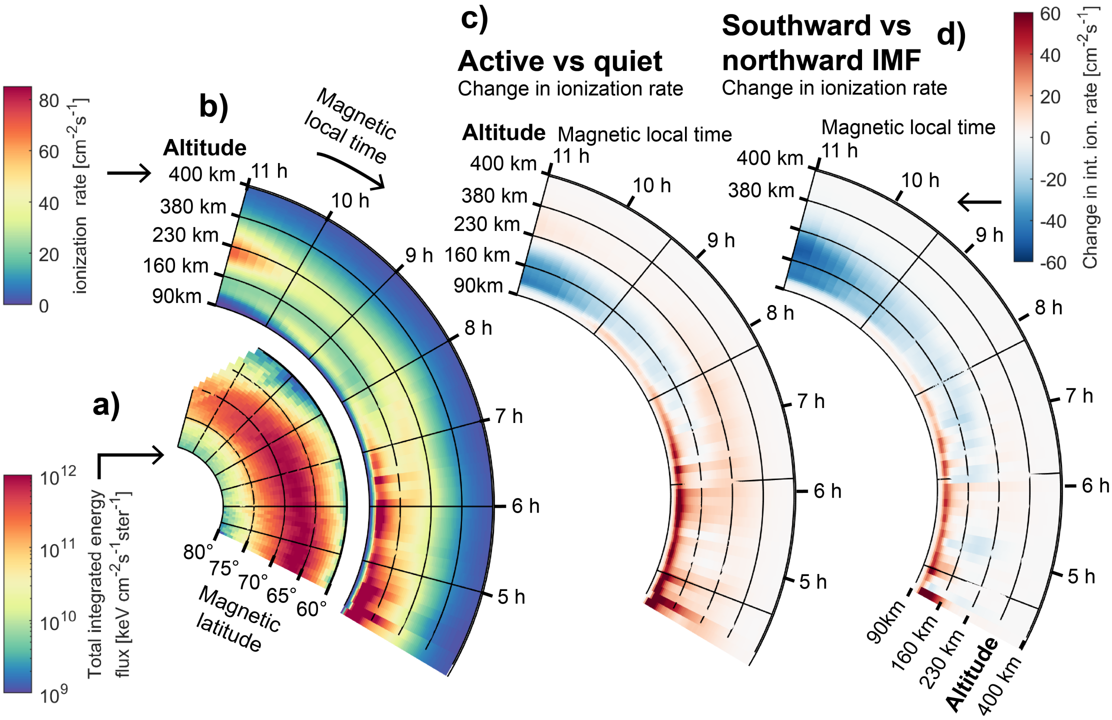

Figure 3. Panel a) shows total integrated energy flux of precipitating electrons and ions, binned by magnetic latitude (radial direction) and magnetic local time (azimuthal direction), based on 5 million precipitating particle spectra from the dawn-sector during northern hemisphere winter, when solar EUV photoionization is minimal, using data gathered during geomagnetically active conditions (defined as measurement times when the auroral electrojet SME-index exceeds 150 nT). **Panel b)** shows the resulting altitude profiles (radial direction) of ionization rate, binned by magnetic local time (azimuthal direction). **Panel c)** shows the E- to F-region ionization ratio, assuming 170 km to be the boundary between those regions, a deliminator that follows the transition from O_2^+, NO^+-dominance to O^+-dominance in the ionosphere Prölss (2004a, b), for each magnetic local time bin. **Panels c) and d)** the contrasts, defined as quiet subtracted from active (c) and southward subtracted from northward interplanetary magnetic field (IMF) configuration, based on bins of the data displayed in panel b). Note that ‘southward and ‘northward´ IMF configuration are defined as delineated by the bottom and top thirds of the ensemble while ‘active´ and ‘quiet´ are delineated by the median.

https://doi.org/10.5194/egusphere-2025-3068
Preprint. Discussion started: 14 July 2025

red indicates the excess ionization rate experienced during disturbed geomagnetic conditions, and where blue color indicates a *reduction* compared to geomagnetic quiet times (this time using the median value of 150 nT as deliminator). Figure 3d) presents the same comparison, this time between southward and northward configurations of the interplanetary magnetic field (with red color indicating excess ionization during a southward field configuration).

Together, the four panels of Figure 3 demonstrate that elevated levels of high-energy particle precipitation at dawn are accompanied by a decrease in such particle precipitation towards noon, causing what appears to be *a tilt* (in magnetic local time) of the entire bottomside ionosphere during geomagnetic active times. Figure 4 explores this trend further, now showing altitude profiles for selected magnetic local times bins (a–e) as well as five geomagnetic activity bins in the noon-sector. The former expound on the trend that a deepening (lowering of the peak ionization altitude) of the ionization rates during active times at earlier local magnetic times are opposed by a raising, or altitude-increase, in ionization rates in the noon-sector during geomagnetic disturbances. In fact, for the most extreme geomagnetic activity bin (top quintile in the SME-index), ionization below 150 km is almost completely absent in the noon-sector.

Next, we shall consider the tendency of the DMSP F18 satellite to consistently orbit through the noon-sector from the poleward-afternoon-side to the equatorward-morning-side of the cusp. This tendency is naturally exploited in a superposed epoch scheme, comparing the median observations of ensembles of orbits. Figure 5a–c) detail some 352 conjunctions between the DMSP F18 satellite and ground-based GNSS receivers on Svalbard, Norway, during which the cusp was directly inferred in the data. Figure 5d–g) show two superposed epoch analyses, for both quiet and active conjunctions, where we compare the occurrence of GNSS phase scintillations with observed ion drift speeds & the inferred ratio of E- to F-region conductance (Eq. 1).

The superposed epoch analysis in Figure 5 reveals a clear, characteristic pattern in the inferred ratio of E- to F-region conductance, η, where the poleward edge of the cusp marks the edge of a region in which E-region ionization is almost absent, leading to very low values of η (~ 0.25). On the other hand, the equatorward edge of the cusp marks the onset of a distinct high-η region (> 0.7): this is the characteristic diffuse aurora that we typically find equatorward of the cusp (Newell et al., 2010; Ivarsen et al., 2024b, 2025c).

4 Discussion

Comparing Figure 5e) and Figure 5g) we observe that the low-η region poleward of the cusp is accompanied elevated occurrence rates of phase scintillations. This action is caused by the proliferation of polar cap patches (Jin et al., 2014), drifting poleward from the cusp, for example created by a tongue-of-ionization action (Hosokawa et al., 2010) or seeded by poleward-moving auroral forms (Frey et al., 2019). The growth of turbulence on the edges of these patches are no doubt aided by low rates of η, which should suppress the ability of the E-region to short-circuit the electric fields that trigger F-region plasma instabilities and accompany irregularities in the plasma (Vickrey and Kelley, 1982; Ivarsen et al., 2021a, 2024b).

Adding to this picture are the ion drift observations shown in Figure 5f–g). These drifts, driven by strong convection electric fields (and the process of dayside reconnection), represent the primary source of free energy that can generate F-region

https://doi.org/10.5194/egusphere-2025-3068
Preprint. Discussion started: 14 July 2025

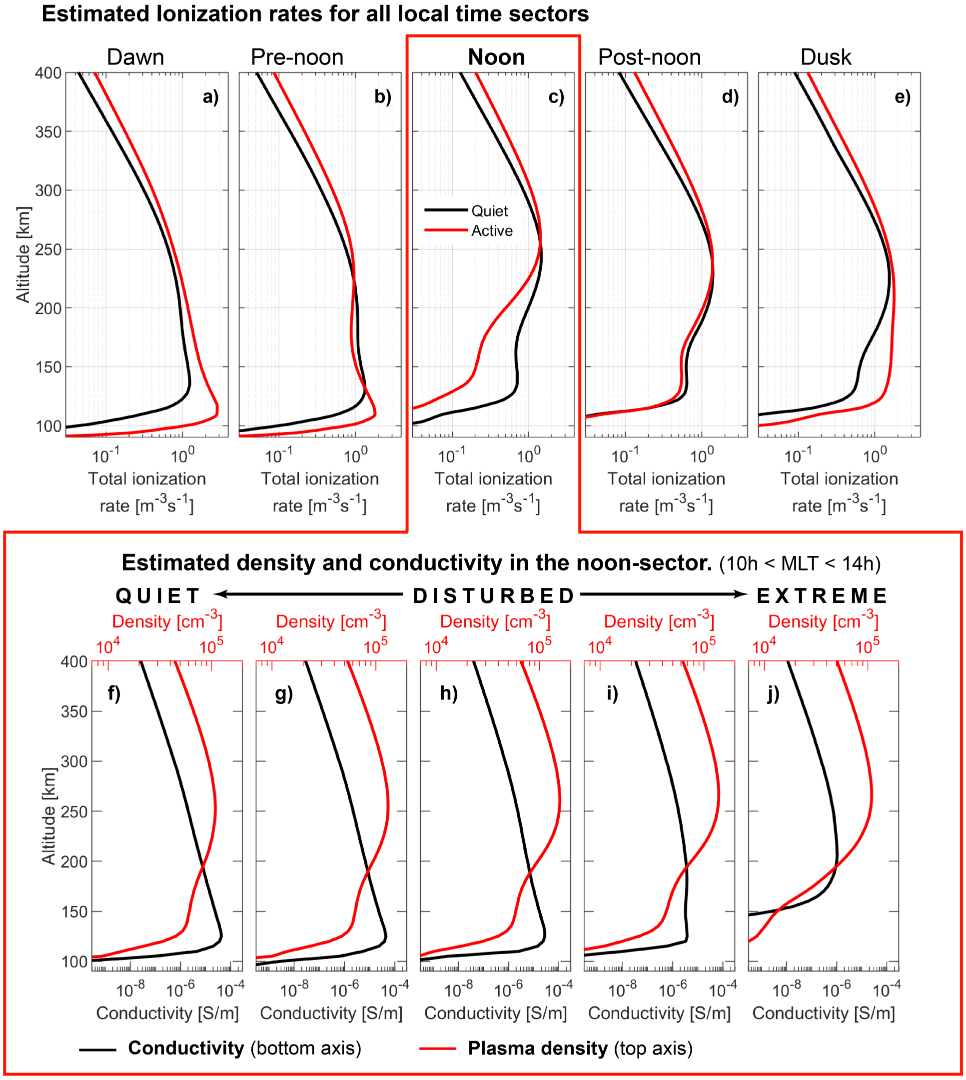

Figure 4. Ionization rate **(panels a–e)** and density & conductivity **(f–j)** profiles, for bins in magnetic local time **(a–e)** and geomagnetic activity **(f–j)**, where the latter five panels show data only from the *noon-sector*. In **panels a–e)**, black and red curve correspond to quiet and active geomagnetic activity level respectively, while in **panels f–j)**, black and red curve denote conductivity and plasma density, respectively, all based on 5 million measurement points made during northern hemisphere winter.

https://doi.org/10.5194/egusphere-2025-3068
Preprint. Discussion started: 14 July 2025

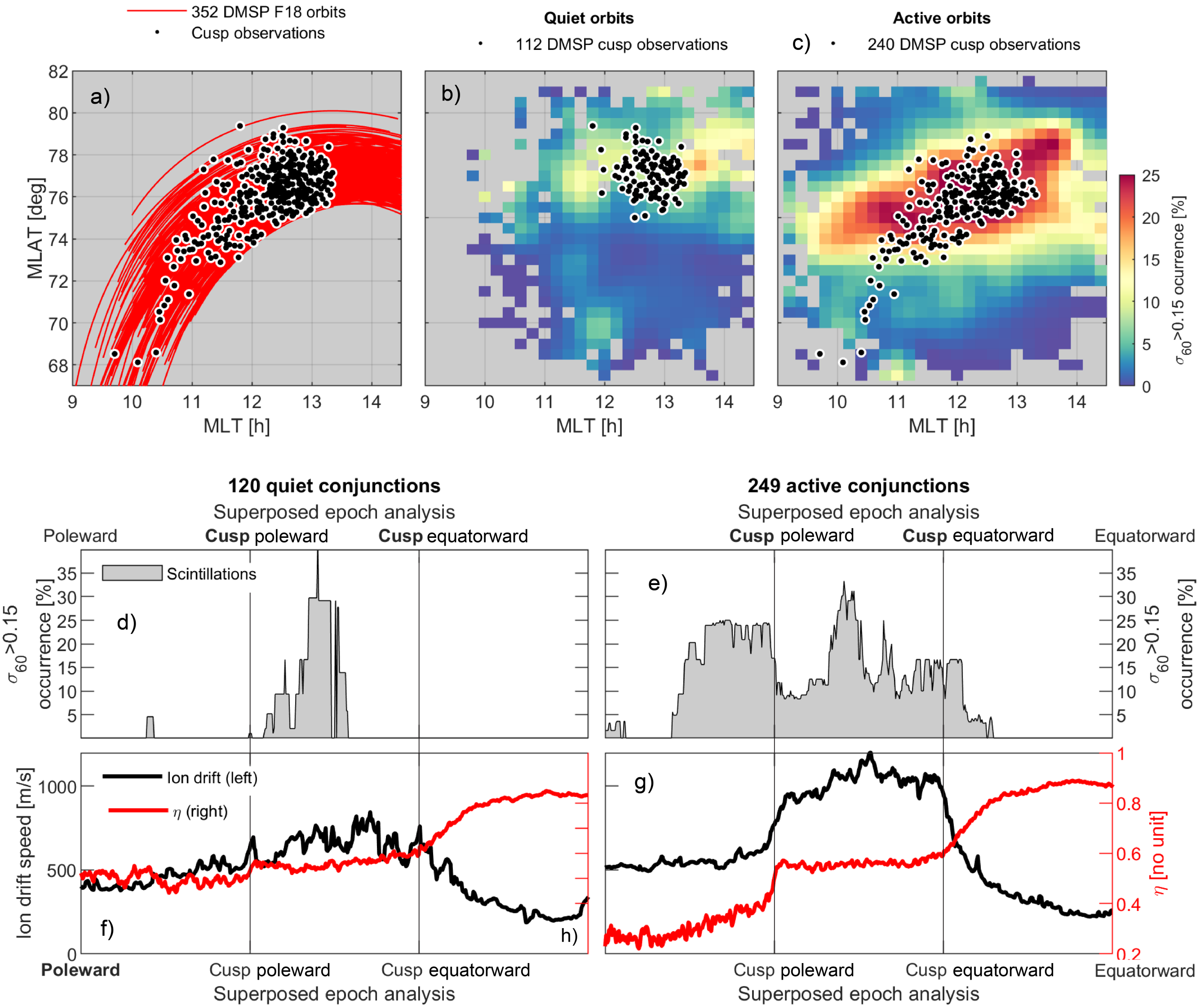

Figure 5. 352 northern hemisphere winter conjunctions between the DMSP F18 satellite and the distributed pierce points implied by three ground-based GNSS receivers, showing orbits where the cusp was identified according to the definitions due to Newell and Meng (1988) **(panel a)**. These conjunctions are divided into quiet- (SME $<$ 70 nT, **panel b**) and active-time (SME $>$ 200 nT, **panel c**) aggregates, superposed on the spatial occurrence rate of phase scintillation events in the surrounding region. In **panels d–e)** the occurrence rate of phase scintillations in the region is shown for the quiet (d) and active (e) conjunctions, now in a superposed epoch analysis, with the poleward and equatorward edges of the cusp stretched to match across the superposed epochs. An equal portion of each orbit is used for the three segments. **Panels f–g)** show the same superposed epoch analysis, this time displaying the cross-track ion drift speeds observed during the orbits (black) and η, the ratio of E- to F-region conductance (Eq. 1).

https://doi.org/10.5194/egusphere-2025-3068
Preprint. Discussion started: 14 July 2025

irregularities in the region. Notably, the drift speeds are highest not poleward or equatorward of the cusp, but directly *inside it*, peaking where the conductance ratio η is transitioning from low to high values. This allows us to view the cusp as an "instability factory": it is the region that combines the strongest driver (electric fields; see, e.g., Tsunoda, 1988) with a relatively weak inhibitor (decreasing η values). The irregularities generated here then convect poleward into a region where, although the drift speed is lower, the inhibitor is almost nonexistent (η is at its lowest). This allows the turbulence to persist for long periods as it populates the polar cap. Conversely, equatorward of the cusp, both the driver (drift speed) and the turbulence itself are suppressed, the latter due to the very high η values that efficiently short-circuit any instability. Whereas This dynamic interplay between the convection driver and the E-region conductance inhibitor is entirely consistent with observations and inferences of the irregularity landscape poleward of the cusp (Jin et al., 2017).

A key aspect of the prevailing picture is the decrease, or even collapse, in energetic particle precipitation inside the noon-sector. It would then seem that the energetic particle precipitation from the radiation belts that normally sustain the dark, dayside E-region (Spasojevic and Inan, 2010; Nishimura et al., 2013; Ni et al., 2014) are effectively drained out from the cusp-region, consistent with recent observations (Ivarsen et al., 2023).

On the other hand, Figure 4 shows that while the E-region at noon collapses, the E-region at dawn and dusk is significantly enhanced during active times, and especially so for the dawn sector. This reflects the substorm cycle, in which energetic particles injected near midnight drift around Earth, eastward towards dawn (Kamide and Kokubun, 1996), providing a robust source of hot electrons that precipitate owing to pitch-angle scattering (Thorne et al., 2010), evident as the eastward "sagging" of the ionosphere evident in Figure 4.

At our onset, Figure 2 illustrated a well-known fact, namely that lower conductivities in the ionosphere is generally associated with an increase in the detrimental effects caused by high-latitude plasma turbulence. Figures 3–5, then, present more complicated, composite trends in the specific degree of ionization in the high-latitude ionosphere implied by particle precipitation. There, numerous chemical and electrodynamic factors are important, but are broadly simplified in the present paper. As such, our albeit interesting and somewhat surprising results must be interpreted with caution, and more thorough investigations of their validity and ramification must follow. Here, we recommend the use of extensive magnetosphere-ionosphere coupling models that take kinetic processes near Earth's radiation belts into account.

5 Conclusions

We have applied fast parameterizations of ionization rate altitude profiles due to Fang et al. (2010) and Fang et al. (2010) to a large database of precipitating particle observations from the high-latitude, northern hemisphere ionosphere, observed during local winter. The efforts have yielded several characteristic trends in the altitude-dependent ionization rate, distinguishing between magnetic local times and various levels of geomagnetic activity. While the calculations at times are based on a wide array of simplifications (the characteristic development in η on display in Figure 5, for example), the trends uncovered are clear and convincing.

https://doi.org/10.5194/egusphere-2025-3068
Preprint. Discussion started: 14 July 2025

The present paper has been an exposition on a recurring question in the mind of the author: is high-energy particle precipitation a sink or source of irregularities in the high-latitude ionosphere? An answer based on the specific and narrowly defined situations considered here is seemingly that the absence of energetic particle precipitation consistently lead to the occurrence of F-region irregularities. However, earlier forays have shown that energetic particle precipitation is directly associated with plasma turbulence (Ivarsen et al., 2024b), capable of embedding structure directly into the ionospheric plasma by merit of field-aligned current filamentation (Ivarsen et al., 2024a), albeit in an intermittent and highly localized manner (Ivarsen et al., 2025b, a).

Data availability. SuperMAG data can be accessed at https://supermag.jhuapl.edu/mag/. Precipitating particle data from DMSP SSJ can be accessed through Madrigal (http://cedar.openmadrigal.org/). GNSS scintillation data from Svalbard are organized with the following nine DOIs. Receiver at Bjørnøya: 10.18710/CMZEWF (2014), 10.18710/QG9XCM (2015), 10.18710/BPU1RV (2016). Kjell Henriksen receiver: 10.18710/LZX3MU (2014), 10.18710/13FHF9 (2015), 10.18710/1CA1KO (2016). Receiver at Ny Ålesund: 10.18710/P69VFS (2014), 10.18710/MIUYBH (2015), 10.18710/D46B20 (2016). Interplanetary magnetic field observations and various geomagnetic indices from NASA's OMNI service can be accessed at https://omniweb.gsfc.nasa.gov/.

Appendix A: Some details on the Method

We use a database of precipitating electron data from the SSJ instrument on the F16, F17, F18, and F19 satellites of the DMSP. The DMSP satellites are in helio-synchronous dawn-dusk 800 km-altitude polar orbits covering most of the dayside high-latitude ionosphere in the northern hemisphere. The SSJ instrument uses particle detectors to measure the energy flux of precipitating electrons and ions through 19 energy channels from 30 eV to 30 keV, with a cadence of 1 second Redmon et al. (2017). The DMSP satellites' orbits cover the high-latitude northern hemisphere dayside, with no coverage in the midnight sector between 21h and 3h.

Example precipitating particle spectra are presented in Figure 1a, and what follows is a detailed explanation of the steps that lead to Figure 1b–d).

A1 From Particle Spectra to Ionization Rate

Each of the 19 energy channels from the DMSP SSJ instrument is treated as a monoenergetic beam, and the resulting ionization rate profiles that are obtained by an implementation of Fang et al. (2010) and Fang et al. (2013) are summed to get the total profile shown in Figure 1b. The state of the neutral atmosphere is captured by the A_P- and $F_{10.7}$-indices, and we use average, pre-calculated model atmospheres based on representative solar local times and latitudes.

https://doi.org/10.5194/egusphere-2025-3068
Preprint. Discussion started: 14 July 2025

A2 From Ionization Rate to Electron Density

Under conditions of darkness (no solar EUV photoionization), the steady-state electron density n_e in the E-region is determined by the balance between production (ionization rate) and loss (recombination), and we assume that NO_+ dominates in the E-region. That gives a plasma density equal to the square root of the ionization rate divided by the recombination rate of NO_+ (Prölss, 2004a, b),

$$n_e = \sqrt{\frac{q}{\alpha}}, \tag{A1}$$

with q being ionization rate, α being recombination rate, and n_e plasma density. We use values for α from Sheehan and St.-Maurice (2004). This gives a density profile in the E-region and lower F-region. From the F-peak, we apply the Chapman-α equation upwards, using ionized gas scale heights from an empirical model due to Li et al. (2019).

A3 From Electron Density to Pedersen Conductivity

Based on the estimated plasma density profile, we exploit expressions for ion-neutral and neutral-neutral collision rates to estimate Pedersen conductivity, following Ivarsen et al. (2021a). In short, we use expressions for collision interaction terms between all charged particles associated with the ion species in the ionosphere, as presented in Schunk and Nagy (1980). Then, we use the International Reference Ionosphere model (IRI) for the ionospheric ion species *proportions*, using the DMSP-estimated plasma density to determine species densities. IRI also provide electron temperature (Alken et al., 2021), we use MSIS for the neutral number densities, and IGRF for the magnetic field strength (Thébault et al., 2015). Although the many models doubtless influence the final density and conductivity values greatly, the main source of variability in our result stem from variability in the precipitating energy flux.

Pedersen conductivity is then arrived at via,

$$\sigma_P = \frac{n_e e^2}{m_i}\left(\frac{\nu_{in}}{\nu_{in}^2+\Omega_i^2}\right) + \frac{n_e e^2}{m_e}\left(\frac{\nu_{en}}{\nu_{en}^2+\Omega_e^2}\right), \tag{A2}$$

where σ_P is the Pedersen conductivity, e is the elementary charge, $m_{i,e}$ are the ion and electron masses, respectively, $\nu_{in,en}$ are the ion-neutral and electron-neutral collision frequencies, respectively, and $\Omega_{i,e}$ are the ion and electron gyrofrequencies, respectively. We then calculate the conductances that enter into Eq. (1), by integrating Pedersen conductivity in the E- and F-regions,

$$\Sigma_{\mathrm{E,F}} = \int\limits_{\mathrm{E,F}} \sigma(h)\, dh. \tag{A3}$$

E-region conductance is dominated by ionization at the nominal Pedersen conductivity peak, which we take as near 140 km, with falling conductivity towards 170 km (Kwak and Richmond, 2007). The transition height between the E- and F-region differ, and we conservatively take 170 km to be the boundary, which roughly matches the transition from O_2^+, NO^+-dominance to O^+-dominance Prölss (2004a, b).

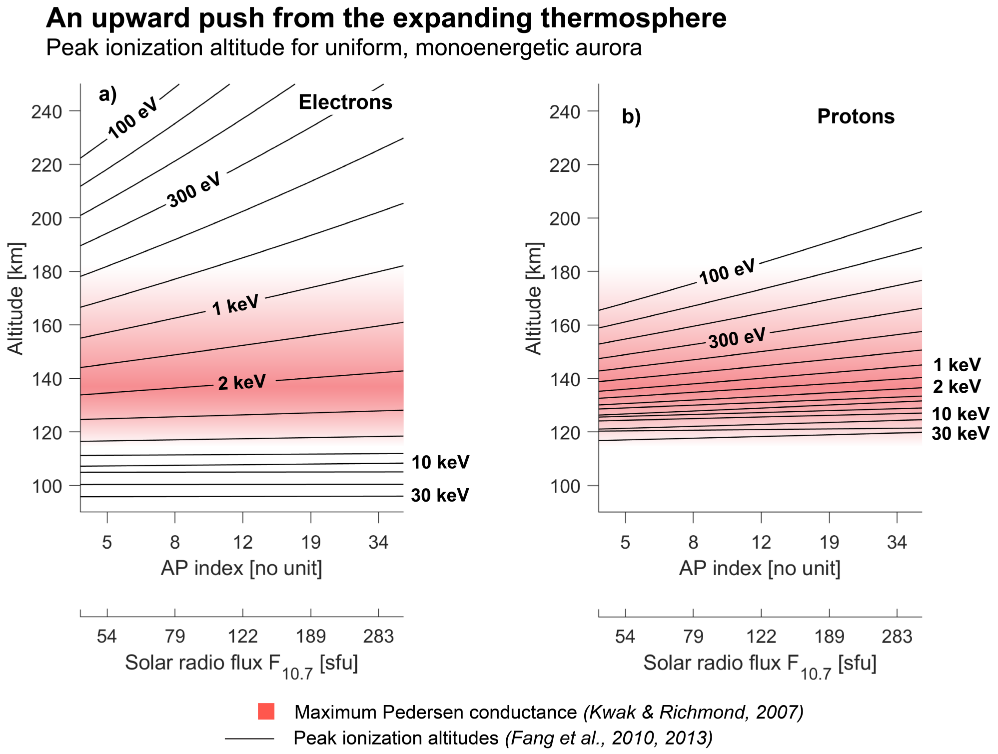

Figure A1. Peak ionization altitudes for uniform monoenergetic electrons (a) and protons (b) for 120 MSIS-based model atmospheres. The y-axis shows altitude and the x-axis shows the AP-index and $F_{10.7}$ solar radio flux values upon which the model atmospheres are based. Each black line represents the peak altitude for particles with energies ranging from 100 eV to 30 keV, while red shaded regions indicate the altitude range at which Pedersen conductance normally maximizes, from Kwak and Richmond (2007).

A4 The Compounding Effect of Thermospheric Neutral Density

The MSIS model, upon whose foundation the Fang et al. (2010) and Fang et al. (2013) parametrizations are implemented in the present paper, accounts for the atmospheric expansion during geomagnetic storms. This important notion, that the thermosphere heats up and expands during storms in geospace, can be quantified.

This physical process works in concert with the changing particle spectra: for any given energy, a particle will be stopped at a higher altitude, owing to increased densities at higher altitudes. This "swelling" of the atmosphere would, by itself, tend to raise the ionization profile and slightly *decrease* the η conductance ratio. This effect likely complements the much more dramatic effect of the spectral changes, and contributes to a deeper, more nuanced understanding of the coupled system.

Figure A1 quantifies the effect, by keeping precipitating particle spectra uniform and constant, varying only the A_P- and $F_{10.7}$-indices. In critical situations, say, cases of extreme thermospheric swelling, the effect may influence the closing of magnetospheric current systems and the charge-carrier mobility that supports such currents. The topic should be investigated further, in future holistic models of the coupled atmosphere-ionosphere-magnetosphere system.

Author contributions. MFI performed the data analysis and wrote the manuscript.

215 *Competing interests.* The author have no competing interests.

Acknowledgements. This work is supported by the European Space Agency's Living Planet Grant No. 1000012348. The author is grateful to Y. Jin, J. Park, JP St-Maurice, L. Clausen, and D. Billett for stimulating discussions.

References

Alken, P., Thébault, E., Beggan, C. D., Amit, H., Aubert, J., Baerenzung, J., Bondar, T. N., Brown, W. J., Califf, S., Chambodut, A., Chulliat, A., Cox, G. A., Finlay, C. C., Fournier, A., Gillet, N., Grayver, A., Hammer, M. D., Holschneider, M., Huder, L., Hulot, G., Jager, T., Kloss, C., Korte, M., Kuang, W., Kuvshinov, A., Langlais, B., Léger, J.-M., Lesur, V., Livermore, P. W., Lowes, F. J., Macmillan, S., Magnes, W., Mandea, M., Marsal, S., Matzka, J., Metman, M. C., Minami, T., Morschhauser, A., Mound, J. E., Nair, M., Nakano, S., Olsen, N., Pavón-Carrasco, F. J., Petrov, V. G., Ropp, G., Rother, M., Sabaka, T. J., Sanchez, S., Saturnino, D., Schnepf, N. R., Shen, X., Stolle, C., Tangborn, A., Tøffner-Clausen, L., Toh, H., Torta, J. M., Varner, J., Vervelidou, F., Vigneron, P., Wardinski, I., Wicht, J., Woods, A., Yang, Y., Zeren, Z., and Zhou, B.: International Geomagnetic Reference Field: The Thirteenth Generation, Earth, Planets and Space, 73, 49, https://doi.org/10.1186/s40623-020-01288-x, 2021.

Baker, K. B. and Wing, S.: A New Magnetic Coordinate System for Conjugate Studies at High Latitudes, Journal of Geophysical Research: Space Physics, 94, 9139–9143, https://doi.org/10.1029/JA094iA07p09139, 1989.

Borovsky, J. E., Birn, J., Echim, M. M., Fujita, S., Lysak, R. L., Knudsen, D. J., Marghitu, O., Otto, A., Watanabe, T.-H., and Tanaka, T.: Quiescent Discrete Auroral Arcs: A Review of Magnetospheric Generator Mechanisms, Space Science Reviews, 216, 1, https://doi.org/10.1007/s11214-019-0619-5, 2019.

Cowley, S. W. H.: TUTORIAL: Magnetosphere-Ionosphere Interactions: A Tutorial Review, Washington DC American Geophysical Union Geophysical Monograph Series, 118, 91, https://doi.org/10.1029/GM118p0091, 2000.

Fang, X., Randall, C. E., Lummerzheim, D., Wang, W., Lu, G., Solomon, S. C., and Frahm, R. A.: Parameterization of Monoenergetic Electron Impact Ionization, Geophysical Research Letters, 37, https://doi.org/10.1029/2010GL045406, 2010.

Fang, X., Lummerzheim, D., and Jackman, C. H.: Proton Impact Ionization and a Fast Calculation Method, Journal of Geophysical Research: Space Physics, 118, 5369–5378, https://doi.org/10.1002/jgra.50484, 2013.

Frey, H. U., Han, D., Kataoka, R., Lessard, M. R., Milan, S. E., Nishimura, Y., Strangeway, R. J., and Zou, Y.: Dayside Aurora, Space Science Reviews, 215, 51, https://doi.org/10.1007/s11214-019-0617-7, 2019.

Hosokawa, K., Tsugawa, T., Shiokawa, K., Otsuka, Y., Nishitani, N., Ogawa, T., and Hairston, M. R.: Dynamic Temporal Evolution of Polar Cap Tongue of Ionization during Magnetic Storm, Journal of Geophysical Research: Space Physics, 115, https://doi.org/10.1029/2010JA015848, 2010.

Ivarsen, M., Huyghebaert, D., Jin, Y., Miyashita, Y., St.-Maurice, J.-P., Hussey, G., Dan, B., Kasahara, S., Song, K., Jayachandran, P., Yokota, S., Miyoshi, Y., Kasahara, Y., Shinohara, I., and Matsuoka, A.: Transient, Turbulent Hall Currents in the Sunlit Terrestrial Ionosphere, https://doi.org/10.21203/rs.3.rs-5313766/v2, 2025a.

Ivarsen, M. F., Jin, Y., Spicher, A., and Clausen, L. B. N.: Direct Evidence for the Dissipation of Small-Scale Ionospheric Plasma Structures by a Conductive E Region, Journal of Geophysical Research: Space Physics, 124, 2935–2942, https://doi.org/10.1029/2019JA026500, 2019.

Ivarsen, M. F., Jin, Y., Spicher, A., Miloch, W., and Clausen, L. B. N.: The Lifetimes of Plasma Structures at High Latitudes, Journal of Geophysical Research: Space Physics, 126, e2020JA028 117, https://doi.org/10.1029/2020JA028117, 2021a.

Ivarsen, M. F., St-Maurice, J.-P., Jin, Y., Park, J., Miloch, W., Spicher, A., Kwak, Y.-S., and Clausen, L. B. N.: Steepening Plasma Density Spectra in the Ionosphere: The Crucial Role Played by a Strong E-Region, Journal of Geophysical Research: Space Physics, 126, e2021JA029 401, https://doi.org/10.1029/2021JA029401, 2021b.

https://doi.org/10.5194/egusphere-2025-3068
Preprint. Discussion started: 14 July 2025

Ivarsen, M. F., Jin, Y., Spicher, A., St-Maurice, J.-P., Park, J., and Billett, D.: GNSS Scintillations in the Cusp, and the Role of Precipitating Particle Energy Fluxes, Journal of Geophysical Research: Space Physics, 128, e2023JA031 849, https://doi.org/10.1029/2023JA031849, 2023.

Ivarsen, M. F., Gillies, M. D., Huyghebaert, D. R., St-Maurice, J.-P., Lozinsky, A., Galeschuk, D., Donovan, E., and Hussey, G. C.: Turbulence Embedded Into the Ionosphere by Electromagnetic Waves, Journal of Geophysical Research: Space Physics, 129, e2023JA032 310, https://doi.org/10.1029/2023JA032310, 2024a.

Ivarsen, M. F., St-Maurice, J.-P., Jin, Y., Park, J., Buschman, L. M., and Clausen, L. B.: To What Degree Does the High-Energy Aurora Destroy F-region Irregularities?, Frontiers in Astronomy and Space Sciences, 11, https://doi.org/10.3389/fspas.2024.1309136, 2024b.

Ivarsen, M. F., Miyashita, Y., St-Maurice, J.-P., Hussey, G. C., Pitzel, B., Galeschuk, D., Marei, S., Horne, R. B., Kasahara, Y., Matsuda, S., Kasahara, S., Keika, K., Miyoshi, Y., Yamamoto, K., Shinbori, A., Huyghebaert, D. R., Matsuoka, A., Yokota, S., and Tsuchiya, F.: Characteristic E-Region Plasma Signature of Magnetospheric Wave-Particle Interactions, Physical Review Letters, 134, 145 201, https://doi.org/10.1103/PhysRevLett.134.145201, 2025b.

Ivarsen, M. F., St-Maurice, J.-P., Hussey, G. C., McWilliams, K., Jin, Y., Clausen, L. B. N., Huyghebaert, D. R., Miyashita, Y., and Sibeck, D.: A Parallel-plate Capacitor-Effect in Earth's Dayside Ionosphere, https://doi.org/10.48550/arXiv.2501.03174, 2025c.

Jin, Y., Moen, J. I., and Miloch, W. J.: GPS Scintillation Effects Associated with Polar Cap Patches and Substorm Auroral Activity: Direct Comparison, Journal of Space Weather and Space Climate, 4, A23, https://doi.org/10.1051/swsc/2014019, 2014.

Jin, Y., Moen, J. I., Oksavik, K., Spicher, A., Clausen, L. B. N., and Miloch, W. J.: GPS Scintillations Associated with Cusp Dynamics and Polar Cap Patches, Journal of Space Weather and Space Climate, 7, A23, https://doi.org/10.1051/swsc/2017022, 2017.

Kamide, Y. and Kokubun, S.: Two-Component Auroral Electrojet: Importance for Substorm Studies, Journal of Geophysical Research: Space Physics, 101, 13 027–13 046, https://doi.org/10.1029/96JA00142, 1996.

Kasahara, S., Miyoshi, Y., Yokota, S., Mitani, T., Kasahara, Y., Matsuda, S., Kumamoto, A., Matsuoka, A., Kazama, Y., Frey, H. U., Angelopoulos, V., Kurita, S., Keika, K., Seki, K., and Shinohara, I.: Pulsating Aurora from Electron Scattering by Chorus Waves, Nature, 554, 337–340, https://doi.org/10.1038/nature25505, 2018.

Kintner P. M., Ledvina B. M., and de Paula E. R.: GPS and Ionospheric Scintillations, Space Weather, 5, https://doi.org/10.1029/2006SW000260, 2007.

Kivanc and Heelis, R. A.: Spatial Distribution of Ionospheric Plasma and Field Structures in the High-Latitude F Region, Journal of Geophysical Research, 103, 6955–6968, https://doi.org/10.1029/97JA03237, 1998.

Kwak, Y.-S. and Richmond, A. D.: An Analysis of the Momentum Forcing in the High-Latitude Lower Thermosphere, Journal of Geophysical Research: Space Physics, 112, https://doi.org/10.1029/2006JA011910, 2007.

Li, Q., Liu, L., Jiang, J., Li, W., Huang, H., Yu, Y., Li, J., Zhang, R., Le, H., and Chen, Y.: Alpha-Chapman Scale Height: Longitudinal Variation and Global Modeling, Journal of Geophysical Research: Space Physics, 124, 2083–2098, https://doi.org/10.1029/2018JA026286, 2019.

Lysak, R., Echim, M., Karlsson, T., Marghitu, O., Rankin, R., Song, Y., and Watanabe, T.-H.: Quiet, Discrete Auroral Arcs: Acceleration Mechanisms, Space Science Reviews, 216, 92, https://doi.org/10.1007/s11214-020-00715-5, 2020.

Meziane, K., Hamza, A. M., and Jayachandran, P. T.: Turbulence Signatures in High-Latitude Ionospheric Scintillation, Journal of Geophysical Research: Space Physics, 128, e2022JA030 934, https://doi.org/10.1029/2022JA030934, 2023.

Moen, J. and Brekke, A.: The Solar Flux Influence on Quiet Time Conductances in the Auroral Ionosphere, Geophysical Research Letters, 20, 971–974, https://doi.org/10.1029/92GL02109, 1993.

Newell, P. T. and Meng, C.-I.: The Cusp and the Cleft/Boundary Layer: Low-altitude Identification and Statistical Local Time Variation, Journal of Geophysical Research: Space Physics, 93, 14 549–14 556, https://doi.org/10.1029/JA093iA12p14549, 1988.

Newell, P. T., Sotirelis, T., and Wing, S.: Diffuse, Monoenergetic, and Broadband Aurora: The Global Precipitation Budget, Journal of Geophysical Research: Space Physics, 114, https://doi.org/10.1029/2009JA014326, 2009.

Newell, P. T., Sotirelis, T., and Wing, S.: Seasonal Variations in Diffuse, Monoenergetic, and Broadband Aurora, Journal of Geophysical Research: Space Physics, 115, https://doi.org/10.1029/2009JA014805, 2010.

Ni, B., Bortnik, J., Nishimura, Y., Thorne, R. M., Li, W., Angelopoulos, V., Ebihara, Y., and Weatherwax, A. T.: Chorus Wave Scattering Responsible for the Earth's Dayside Diffuse Auroral Precipitation: A Detailed Case Study, Journal of Geophysical Research: Space Physics, 119, 897–908, https://doi.org/10.1002/2013JA019507, 2014.

Nishimura, Y., Bortnik, J., Li, W., Thorne, R. M., Ni, B., Lyons, L. R., Angelopoulos, V., Ebihara, Y., Bonnell, J. W., Le Contel, O., and Auster, U.: Structures of Dayside Whistler-Mode Waves Deduced from Conjugate Diffuse Aurora, Journal of Geophysical Research: Space Physics, 118, 664–673, https://doi.org/10.1029/2012JA018242, 2013.

Picone, J. M., Hedin, A. E., Drob, D. P., and Aikin, A. C.: NRLMSISE-00 Empirical Model of the Atmosphere: Statistical Comparisons and Scientific Issues, Journal of Geophysical Research: Space Physics, 107, SIA 15–1–SIA 15–16, https://doi.org/10.1029/2002JA009430, 2002.

Prikryl, P., Jayachandran, P. T., Chadwick, R., and Kelly, T. D.: Climatology of GPS Phase Scintillation at Northern High Latitudes for the Period from 2008 to 2013, Ann. Geophys., 33, 531–545, https://doi.org/10.5194/angeo-33-531-2015, 2015.

Prölss, G. W.: Absorption and Dissipation of Solar Radiation Energy, in: Physics of the Earth's Space Environment: An Introduction, edited by Prölss, G. W., pp. 77–157, Springer, Berlin, Heidelberg, https://doi.org/10.1007/978-3-642-97123-5_3, 2004a.

Prölss, G. W.: Absorption and Dissipation of Solar Wind Energy, in: Physics of the Earth's Space Environment: An Introduction, edited by Prölss, G. W., pp. 349–399, Springer, Berlin, Heidelberg, https://doi.org/10.1007/978-3-642-97123-5_7, 2004b.

Redmon, R. J., Denig, W. F., Kilcommons, L. M., and Knipp, D. J.: New DMSP Database of Precipitating Auroral Electrons and Ions, Journal of geophysical research. Space physics, 122, 9056–9067, https://doi.org/10.1002/2016JA023339, 2017.

Schunk, R. W. and Nagy, A. F.: Ionospheres of the Terrestrial Planets, Reviews of Geophysics, 18, 813–852, https://doi.org/10.1029/RG018i004p00813, 1980.

Sheehan, C. H. and St.-Maurice, J.-P.: Dissociative Recombination of N2+, O2+, and NO+: Rate Coefficients for Ground State and Vibrationally Excited Ions, Journal of Geophysical Research: Space Physics, 109, https://doi.org/10.1029/2003JA010132, 2004.

Song, K., Hamza, A. M., Jayachandran, P. T., Meziane, K., and Kashcheyev, A.: Spectral Characteristics of Phase Fluctuations at High Latitude, Journal of Geophysical Research: Space Physics, 128, e2022JA031 244, https://doi.org/10.1029/2022JA031244, 2023.

Spasojevic, M. and Inan, U. S.: Drivers of Chorus in the Outer Dayside Magnetosphere, Journal of Geophysical Research: Space Physics, 115, https://doi.org/10.1029/2009JA014452, 2010.

Thébault, E., Finlay, C. C., Beggan, C. D., Alken, P., Aubert, J., Barrois, O., Bertrand, F., Bondar, T., Boness, A., Brocco, L., Canet, E., Chambodut, A., Chulliat, A., Coïsson, P., Civet, F., Du, A., Fournier, A., Fratter, I., Gillet, N., Hamilton, B., Hamoudi, M., Hulot, G., Jager, T., Korte, M., Kuang, W., Lalanne, X., Langlais, B., Léger, J.-M., Lesur, V., Lowes, F. J., Macmillan, S., Mandea, M., Manoj, C., Maus, S., Olsen, N., Petrov, V., Ridley, V., Rother, M., Sabaka, T. J., Saturnino, D., Schachtschneider, R., Sirol, O., Tangborn, A., Thomson, A., Tøffner-Clausen, L., Vigneron, P., Wardinski, I., and Zvereva, T.: International Geomagnetic Reference Field: The 12th Generation, Earth, Planets and Space, 67, 79, https://doi.org/10.1186/s40623-015-0228-9, 2015.

Thomas, E. G. and Shepherd, S. G.: Statistical Patterns of Ionospheric Convection Derived From Mid-latitude, High-Latitude, and Polar SuperDARN HF Radar Observations, Journal of Geophysical Research: Space Physics, 123, 3196–3216, https://doi.org/10.1002/2018JA025280, 2018.

Thorne, R. M., Ni, B., Tao, X., Horne, R. B., and Meredith, N. P.: Scattering by Chorus Waves as the Dominant Cause of Diffuse Auroral Precipitation, Nature, 467, 943–946, https://doi.org/10.1038/nature09467, 2010.

Tsunoda, R. T.: High-Latitude F Region Irregularities: A Review and Synthesis, Reviews of Geophysics, 26, 719–760, https://doi.org/10.1029/RG026i004p00719, 1988.

Vickrey, J. F. and Kelley, M. C.: The Effects of a Conducting E Layer on Classical F Region Cross-Field Plasma Diffusion, Journal of Geophysical Research: Space Physics, 87, 4461–4468, https://doi.org/10.1029/JA087iA06p04461, 1982.

Yeh, K. C. and Liu, C.-H.: Radio Wave Scintillations in the Ionosphere, IEEE Proceedings, 70, 324–360, 1982.